ACS Energy LETTERS

http://pubs.acs.org/journal/aelccp

LETTER

Effect of Microstructure on the Cycling Behavior of Li–In Alloy Anodes for Solid-State Batteries

Jack Aspinall, Yvonne Chart, Hua Guo, Pranay Shrestha, Matthew Burton, and Mauro Pasta*

Cite This: *ACS Energy Lett.* 2024, 9, 578–585

Read Online

ACCESS | Metrics & More | Article Recommendations | Supporting Information

ABSTRACT: **Indium–lithium alloys operating in the two-phase region of indium metal and the InLi intermetallic are the counter and reference electrodes of choice in two-electrode solid-state batteries. At high current densities on both charge and discharge, they offer low polarization, good accessible capacity, and good cycle life. By synthesizing a phase pure InLi intermetallic and measuring its diffusion and mechanical properties, it is clear that the electrochemical performance is attributable to measured fast diffusion kinetics in the InLi intermetallic, $D_{Li}^{298K} = 5.5 \times 10^{-7}$ cm^2 s^{-1}. The indium metal phase is essentially ion-blocking, so the performance is tied to the microstructure, which evolves with cycling. A simple two-layer microstructure is proposed, based on the fundamental understanding established, which maximizes performance. Despite the limitations of indium-based alloys in commercial applications, the lessons learned can be extended to other fast-conducting lithium intermetallics.**

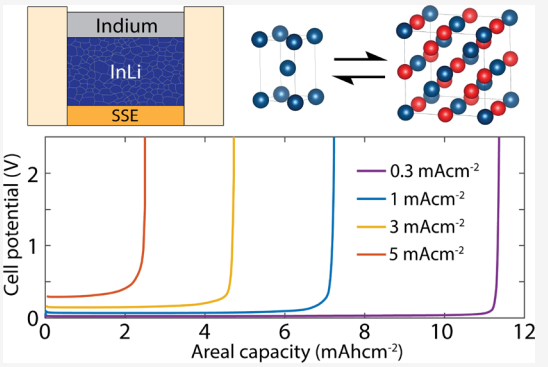

Solid-state battery (SSB) technology incorporating inorganic solid-state electrolytes is an attractive option to power electric vehicles (EVs), primarily as it could enable the safe implementation of high energy density electrodes including lithium metal anodes (theoretical capacity ~3860 mAh g^{-1} and 2061 mAh cm^{-3}).[1] These can lead to cells with gravimetric and volumetric energies upward of 400 Wh kg^{-1} and 1000 Wh L^{-1}, which are thermally stable and amenable to fast charging.[2]

Current generation solid-state batteries have very low critical current densities (current density above which cell shorts occur) when using a lithium metal electrode.[3−5] This is particularly true of solid electrolytes (SE) produced by scaleable methodologies such as tape casting.[6] Current evidence suggests this is due to high electrolyte porosity, which enables solid electrolyte fracture under the stresses generated by lithium metal plating.[7] Solving this issue by advancing solid-state manufacturing of electrolytes, and progressing novel strategies such as interlayers[8] and functionalized current collectors,[9] is important.

In the meantime, the low current densities achievable with a lithium metal electrode are holding back the rate of progress in electrode development,[10] specifically solid-state composite cathodes[11] and initially lithium-free anodes where lithium metal plates on the first charge. Lithium metal has limited diffusion kinetics, readily loses contact with the solid electrolyte, and forms filaments on plating, which leads to cell shorting.[5,12,13] An alternative counter electrode is needed that can cycle relevant capacities at higher current densities, without shorting. This material should form a good reference electrode, with a constant potential over a wide capacity range at a high charge/discharge rate.

The lithium–indium alloy system has gained popularity in this role,[14−16] but there is little understanding of the mechanism underpinning the performance or the limitations of the electrode, preventing the rationally driven optimization of the electrode to maximize its performance. The lack of a fundamental understanding risks misleading conclusions. The region of interest is the wide two-phase region between indium and the InLi intermetallic, which can be seen on the phase diagram in Figure 1A, redrawn from ref 14.

The material properties of the indium metal are relatively well understood. Chemically it is stable, especially compared to other battery materials (E = −0.34 V vs SHE). Mechanically, indium is very similar to lithium,[17] a soft metal (E = 12.7 GPa,

Received: October 24, 2023
Revised: January 18, 2024
Accepted: January 19, 2024
Published: January 26, 2024

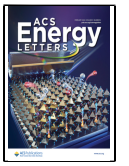

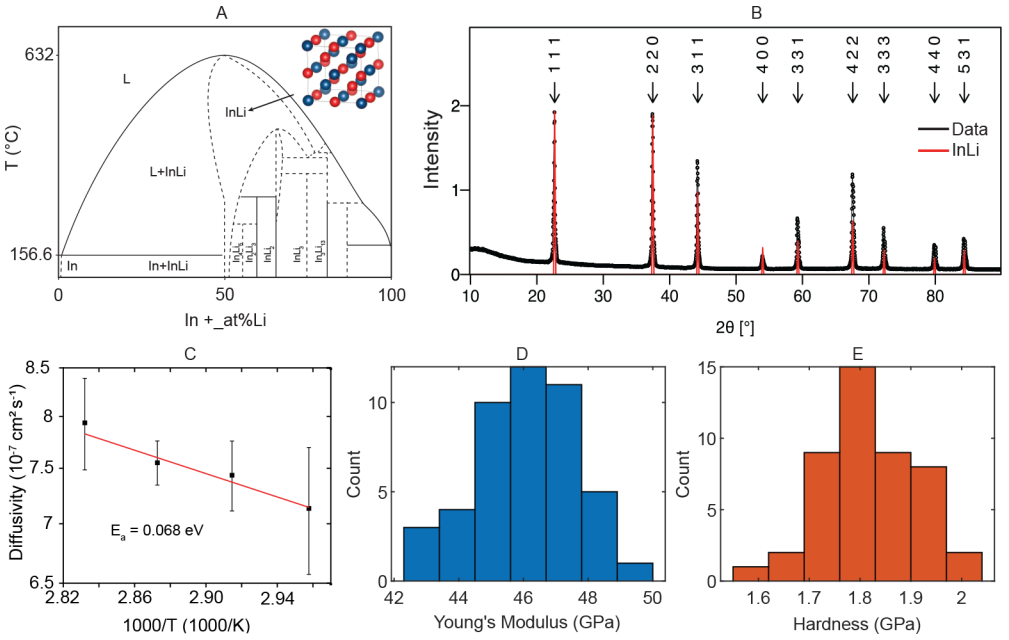

Figure 1. (A) Indium lithium binary phase diagram, redrawn from ref 14. InLi unit cell inset. (B) Powder XRD of hand-milled InLi powder showing phase purity. (C) ^{7}Li PFG-NMR diffusivity as a function of temperature for the InLi intermetallic. (D) InLi modulus histogram from continual stiffness measurement. (E) InLi hardness histogram measured from indentation impression size.

G = 3.8 GPa, ν = 0.45, σ_y = 0.93 MPa), which, due to its low melting point (T_m = 156.6 °C), is prone to creep and stress relaxation.[18] The diffusion kinetics of indium are sluggish, with a bulk self-diffusion coefficient ($D_{self}^{297.6K}$ = 5.7 × 10^{-14} cm^2 s^{-1})[17] which is 3 orders of magnitude lower than lithium's self-diffusivity. Indium's use in practical batteries is limited by its high density of 7.31 g cm^{-3}. The material properties of the second phase in this system, the InLi intermetallic, are poorly understood.

In this study, we investigate the fundamental properties of the InLi intermetallic phase. Then, we investigate the microstructural processes underpinning observed electrochemical performance. The understanding gained is key to developing high-performance lithium-rich alloy anodes.

Material properties of the InLi intermetallic. Phase pure InLi intermetallic was formed by melting and resolidifying a 1:1 stoichiometric mix of indium and lithium metal. It was easily ground to a powder using a pestle and mortar, and the particle size was further reduced by ball milling (Figure S1). The powder XRD taken of the hand-milled powder in Figure 1B shows that the material aligns with the predicted B32 cubic $Fd\bar{3}m$ structure with a unit cell size of 6.788 Å. No impurity peaks were present.

As identified in a previous paper on lithium magnesium alloys,[19] the most fundamental material property influencing electrochemical discharge performance is the rate of lithium diffusion. To this end, the self-diffusion coefficient of InLi was investigated by using ^{7}Li pulsed field gradient nuclear magnetic resonance spectroscopy (PFG-NMR). Diffusivity was measured as a function of temperature, with reliable data observed above 334 K (T_2 < 10 ms, Figure S2). The data between 338 and 354 K were fit with the Arrhenius equation giving a very low activation energy of 0.068 ± 0.037 eV (Figure 1C). The fit extrapolates to give a room temperature (298 K) lithium diffusivity of 5.5 ± 1.0 × 10^{-7} cm$_2$ s^{-1}. Our data shows diffusivity values about a factor of 2 lower than work done by Tarczon et al. in 1988, which reports D_0 values from 7.7 × 10^{-6} to 3.5 × 10^{-5} cm^2 s^{-1} across a range of Li:In compositions (47% to 53% In) due to changes in vacancy concentration, with very similar activation energies of 0.086 to 0.061 eV.[20] For diffusivity measurements taken 35 years apart, these values are in strong agreement. Recent computational work has sought to understand the diffusion mechanism in this intermetallic alongside other indium−lithium intermetallics and the comparable lithium tin system.[21] The work compares two theoretical mechanisms of atom hopping, interstitial diffusion with an activation energy of 0.25 eV and vacancy diffusion with an activation energy of 0.015 eV. Our experimentally observed activation energy of 0.068 eV comprises both the vacancy hopping energy and the vacancy creation energy. Assuming the computational work is accurate, subtracting the hopping energy from our total value gives a vacancy creation activation energy of 0.053 eV. Using the Nernst−Einstein expression where F = 96 485 C mol^{-1}, c_i is the concentration of the diffusing species, 40.4 mmol cm^{-3}, R = 8.31 J mol^{-1} K^{-1}, and T = 303 K; relating diffusivity and ionic conductivity, eq 1, the InLi phase has an ionic conductivity at 303 K of 82.3 mS cm^{-1}.

$$\sigma = \frac{F^2 c_i}{RT} D_i \tag{1}$$

Nanoindentation was performed to quantify the intermetallic's mechanical properties. The values for Young's modulus and hardness for 46 indents are presented in Figure 1D,E. The mean Young's modulus is 46.1 ± 1.4 GPa measured using the continual stiffness measurement (CSM) technique.[22] After indenting, the impression areas were measured by using the scanning electron microscope (SEM) within which the indenter sits. The mean impression size was 14.06 ± 0.66 μm^2, with a mean maximum load of 25.46 ± 0.02 mN. The mean hardness is 1.82 ± 0.08 GPa, approximately twice the 0.921 ± 0.196 GPa of argyrodite solid electrolyte Li_6PS_5Cl.[13] The hardness and modulus measured by the low-load CSM

https://doi.org/10.1021/acsenergylett.3c02274
ACS Energy Lett. 2024, 9, 578−585

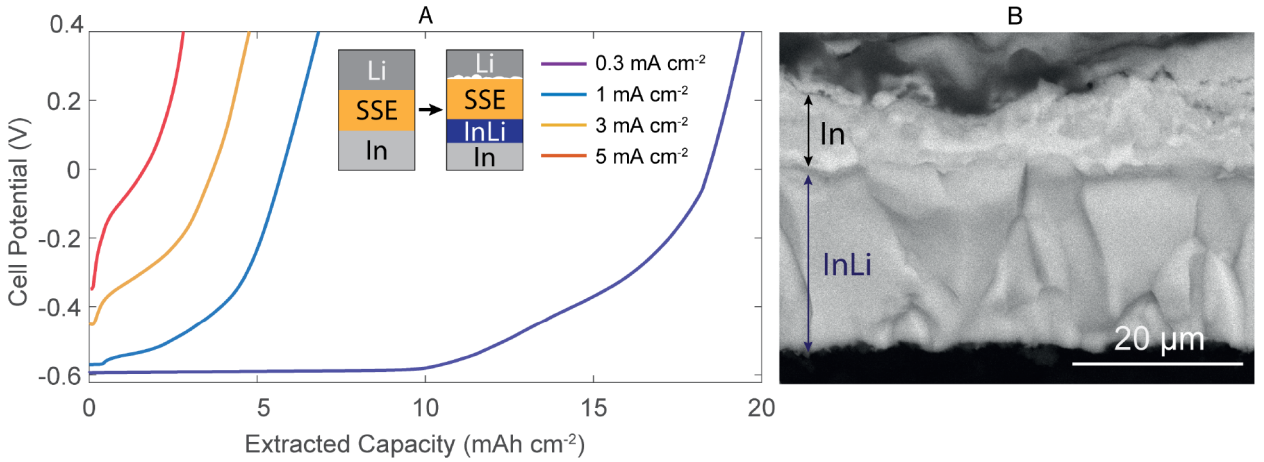

Figure 2. Lithiation of indium metal. (A) Chronopotentiometry showing discharge of lithium metal with an indium metal counter electrode at 30 °C and 5 MPa. Cell schematic before/after test inset. (B) Cross-sectional image of partially lithiated indium metal showing two-phase microstructure.

technique as a function of indent depth are plotted in Figure S3. Measured hardness is essentially independent of depth, as is expected for hard materials. Notably, no indentation fracture was observed either in the load−displacement data or at the corners of the indent impression. This remained true using much larger indentation loads of 500 mN using a sharper cube-corner tip, Figure S4A, suggesting a fracture toughness of at least 5 MPa$\sqrt{m}$. An example indent micrograph is shown in Figure S4B, where clear slip bands corresponding to the $\{\bar{1}01\}$ slip planes, checked using electron backscatter diffraction (EBSD), can be observed. These are typically the active slip planes in cubic intermetallics.[23] The interesting insight here is that under high load at the nanoscale, plasticity is observed, with no clear fracture in either the load−displacement data or the indent micrographs. The plasticity seems limited to a single set of slip planes, leading to very clear slip bands. This is distinct from the macroscopic behavior, where the material is brittle, as the limited number of slip systems do not allow general deformation, leading to stress concentrations at the boundaries where deformation cannot be accommodated. The established mechanical and diffusion properties of the intermetallic underpin the production of electrodes and the observed electrochemical performance.

Indium metal lithiation. Shorting is commonly observed when using lithium metal as a counter electrode, especially at high current densities.[5] This is caused by lithium filaments propagating across the solid electrolyte.[4] The potential of the Li^+/InLi half reaction is 622 mV above Li^+/Li (Figure S5). This high alloying potential is a substantial thermodynamic barrier to lithium metal plating, and therefore, the electrode should be highly resistant to cell shorting. To investigate this, cells were assembled with a lithium metal electrode and an indium metal foil counter electrode. Constant areal current densities between 0.3 and 5 mA cm^{-2} were applied, and the cell potential was monitored over time. Figure 2A shows that the cells ran stably with no shorting.

To investigate the lithiation mechanism, a thin indium foil (20 μm) was lithiated with 2 mAh cm^{-2} of lithium at a current density of 1 mA cm^{-2} in a solid-state cell. On the onset of lithiation, the potential goes to that of the In|InLi two-phase region, plus the cell overpotential,[14] suggesting the solid-solubility limit of lithium in indium is negligible. The cell was disassembled to isolate the electrode for characterization. Figure 2B shows a backscattered electron image of a microtome cross-section of the partially lithiated electrode taken at 45°. A clear two-layer morphology can be observed. The fracture morphology and lower backscattered electron signal intensity of the lower layer suggest that it is InLi, whereas the top layer is primarily indium metal. X-ray diffraction (XRD) of the electrode, shown in Figure S6, shows the sample is primarily InLi, with some indium metal phase. No other phases are present. The two-layer morphology suggests that an InLi-In phase boundary propagates through the electrode thickness as more lithium is added. The very high ionic conductivity of the InLi phase makes indium a near-ideal counter electrode on charge. The ionic conductivity calculated from the NMR data suggests a 160 μm thick InLi layer leads to just 1 mV of electrode overpotential at 5 mA cm^{-2}. Therefore, for all practical thicknesses of this layer and practical currents, it is always favorable to form more InLi from the remaining indium, instead of forming In_4Li_5 (0.34 V vs Li^+/Li[14]) or plating out lithium metal.

As well as demonstrating indium's stability on lithiation, Figure 2A shows that there are substantial overpotentials associated with stripping the lithium metal electrode at high rates in these conditions (30 °C, 5 MPa). At higher current densities, a lower capacity is accessible before the potential rapidly increases. Pure lithium metal clearly does not meet the performance requirements of solid-state batteries, which motivates research into novel anode architectures including alloys.[24]

Indium−lithium electrodes for fast discharge. With the objective of developing an initially lithiated electrode architecture capable of high areal capacity and high rate of discharge for solid-state batteries, a two-layer electrode architecture was obtained by first cold-pressing 70 mg of ball-milled phase pure InLi intermetallic onto the surface of the cold-pressed argyrodite solid electrolyte pellet before attaching an indium metal foil disc to the outer surface.

The use of indium alone is insufficient as it does not return all charged capacity when subsequently discharged, Figure S7. It has been typical to produce lithium indium electrodes by pressing pure indium and lithium metal foils such that the ratio of indium to lithium atoms is just greater than 1.[14,16] Although a solid-state reaction does occur to form the InLi intermetallic (Figure S8), the reaction kinetics are slow, the mass loading is

https://doi.org/10.1021/acsenergylett.3c02274
ACS Energy Lett. 2024, 9, 578−585

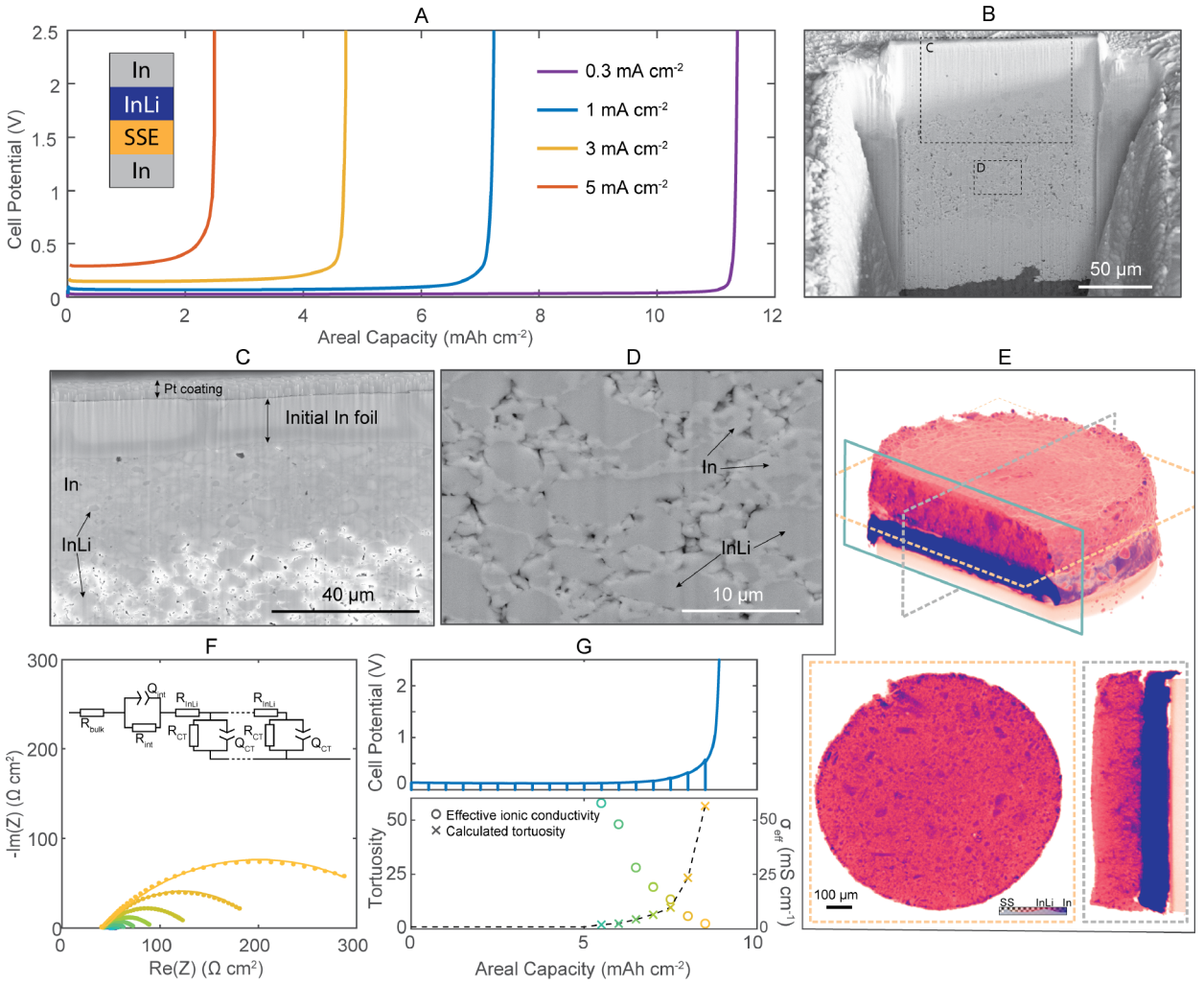

Figure 3. (A) Chronopotentiometric stripping of InLi two-layer electrode at a range of current densities from 0.3 to 5 mA cm^{-2} at 30 °C and 5 MPa with an indium metal counter electrode. Cell schematic inset. (B) Cross-sectional SEM images of 1 mA cm^{-2} lithium depleted electrode, zoomed images for images C−D highlighted. (C−D) Higher-magnification cross-sectional SEM images. (E) X-ray computed tomography reconstructions of InLi electrode after discharge to 2.5 V at 1 mA cm^{-2} current density, showing 3-D reconstructed volume (top, sectioned for clarity) and two representative cross-sectional slices (bottom). (F) Impedance curves collected intermittently throughout discharge at 1 mA cm^{-2}, fit with the inset equivalent circuit. (G) Chronopotentiometry for intermittent impedance test (top) and calculated effective ionic conductivity and tortuosity with areal capacity (bottom).

hard to accurately control, and the electrode potential is unstable. As the intermetallic is hard and nonadhesive, volume contraction during the solid-state reaction can lead to contact loss if lithium is placed on the electrolyte side (Figure S9). If indium is placed on the electrolyte-facing side, the microstructure formed consists of InLi islands within the surface layer, which limits the accessible capacity and limits insight from electrochemical impedance spectroscopy (EIS) due to uncertainty on the active contact area (Figure S9). The intermetallic powder cold-pressing method proposed in this work is, therefore, a superior method for producing high-capacity, high-performance counter electrodes ensuring stable potentials, good contact, and large accessible capacities.

Unidirectional chronopotentiometry was performed, using an indium metal counter electrode at 0.3, 1, 3, and 5 mA cm^{-2}. Measured potential vs extracted areal capacity is plotted in Figure 3A. As can be observed, the extracted capacity is higher than for lithium metal at each current density, and the potential profiles are very flat, before rapidly increasing at the end.

$$\mathrm{InLi}_{(1-x)} \rightarrow (1-x)\mathrm{InLi} + x\mathrm{In} \quad (2)$$

The theoretical capacity of 70 mg of InLi intermetallic is equivalent to 19.9 mAh cm^{-2}. All of the cells deliver below this. As the electrode is discharged, indium metal precipitates nucleate and grow within the InLi layer, leading to the progressive blocking of lithium transport through the electrode; contributing to an increasing observed potential. The potential increase in the two-layer InLi happens at a lower extracted capacity for higher current densities, suggesting the formation of indium precipitates in the InLi matrix is more localized to the surface in these cases. In line with this, at 1 mA cm^{-2} current density, doubling the mass of intermetallic used has no meaningful impact on the extracted capacity (Figure S11).

An electrode cross-section, discharged to the 2.5 V potential limit at 1 mA cm^{-2}, is shown in Figure 3B with zoomed-in images in parts C and D. A thin 20 μm indium foil was used in the cell to reduce the shadowing caused by the plasma focused ion beam (PFIB) trench. The indium phase, which appears

https://doi.org/10.1021/acsenergylett.3c02274
ACS Energy Lett. 2024, 9, 578−585

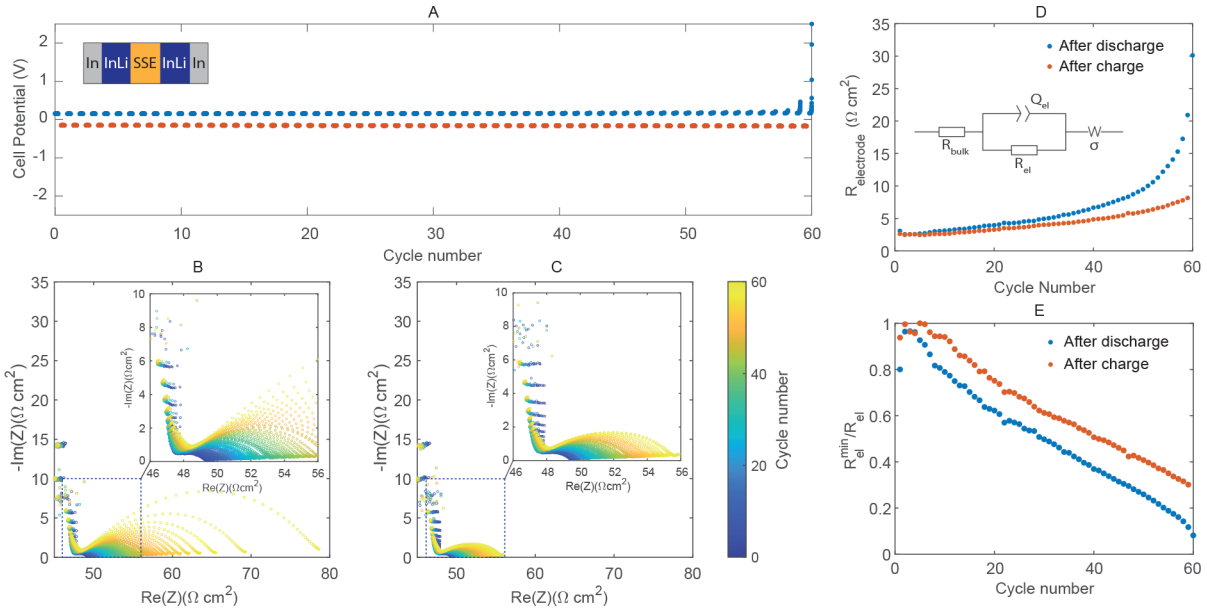

Figure 4. (A) Cycling potentiometry 3 mA cm^{-2}, capacity of 3 mAh cm^{-2} at 30 °C, and 5 MPa for self-symmetric InLilIn two-layer electrodes. Cell schematic inset. (B) EIS data after working electrode discharge. (C) EIS data after working electrode charge. (D) Electrode resistance term over cycles. (E) The ratio of open-circuit electrode resistance to each cycle's electrode resistance.

significantly lighter in the SEM, is observed throughout the electrode. The existing In-InLi interface due to the foil has propagated into the InLi layer. This can be seen most clearly in Figure 3C, where the initial indium foil layer can be distinguished and the former InLi particle boundaries are visible. If all indium formed at this interface, the full capacity could be extracted. In Figure 3D, a two-phase morphology can be seen within the former InLi layer, with a characteristic length scale of around 5 μm. The indium has precipitated on former InLi particle boundaries, as these are lower-energy nucleation sites. Such a tortuous microstructure will decrease the effective ionic conductivity of the material compared with the pristine InLi. The observed porosity can be attributed to the 34% volume contraction associated with the phase transition. Third, a thick layer of indium can be observed at the solid electrolyte interface in Figure 3B. This layer is too thick for lithium to diffuse through, suggesting it is part of a larger surface precipitate. Computed tomography (CT) of a 1 mm diameter cell after discharge at 1 mA cm^{-2} shown in Figure 3E, chronopotentiometry in Figure S12, shows indium precipitates distributed throughout the microstructure.

Cross-sectional imaging demonstrates significant microstructural evolution after electrode discharge throughout the electrode. The mechanism behind the formation of indium metal within the InLi layer is analogous to nucleation from a supersaturated phase, a common phenomenon in metallurgy. Given the initial presence of indium metal, the electrode starts with the InLi phase at the most indium-rich concentration in its solid solution window. Upon removal of lithium from the InLi phase, there is a thermodynamic driving force for phase separation. The precipitation of indium metal from depleted InLi returns the remaining InLi to its equilibrium composition, see eq 2. The kinetics of this phase transformation determine the electrochemical performance. If it were immediate, then an indium layer would instantly form at the interface with the solid electrolyte blocking transport. Were it very slow, the existing indium-InLi phase boundary would propagate, and all the capacity of the InLi layer would be extracted. The reality is somewhere in the middle. The finite kinetics of this phase transformation and high diffusivity of the InLi phase allow a concentration gradient of lithium in the InLi phase to form, which extends deep into the electrode, particularly at low current densities. Indium precipitation is therefore observed throughout the electrode, especially at microstructural defects such as the InLi particle boundaries.

To further investigate indium precipitation throughout the electrode, impedance spectroscopy was conducted after every 0.5 mAh cm^{-2} of lithium was extracted at a current density of 1 mA cm^{-2} on InLi symmetric cells (Figure 3F). To isolate the impedance contribution from the discharged InLi electrode, an indium and lithium coated nickel mesh reference electrode was used, as first reported by Rieger et al.[25] Due to the lack of lithium ion conductivity in indium, the discharging InLi layer impedance spectra component can be fitted with a transmission-line model (TLM) much like a composite cathode.[26−28] The TLM used here (inset in Figure 3F) describes two conduction pathways: ionic through the InLi phase and electronic throughout the electrode. Due to both In and InLi being electrically conductive with minimal boundary resistance and with both having electrical conductivity several orders of magnitude higher than InLi's ionic conductivity, the electrical resistance is assumed to be zero. At low lithium extraction levels, the impedance is dominated by the SE:InLi interface; however, as more lithium is extracted, the tortuosity of the ionic pathway of Li in InLi increases, resulting in a decreased effective ionic conductivity in the electrode, as can be seen in Figure 3G; values are available in Table S1. The tortuosity, calculated from the EIS data using the ionic conductivity from NMR results, consistently increases as more lithium is extracted (Figure 3G), reaching over 50 before the cell potential reaches its limit of 2.5 V. There is a positive feedback loop where as the microstructure becomes more tortuous, the effective ionic conductivity drops, leading to a greater fraction of indium precipitation in the remaining conduction pathways, further increasing the tortuosity. This is particularly the case for higher current densities. The presence of tortuous pathways

https://doi.org/10.1021/acsenergylett.3c02274
ACS Energy Lett. 2024, 9, 578−585

can be observed in CT images, whereby In-rich phases (shown in purple in Figure 3E) are distributed throughout the InLi matrix (shown in deep pink in Figure 3E).

The accessible capacity at high current densities can be increased significantly by the addition of solid electrolyte to form a composite electrode,[29−31] as shown in Figure S13. Due to the comparatively low ionic conductivity of the solid electrolyte compared to the InLi intermetallic, the electrode overpotentials during cycling (3 mA cm^{-2}, 6 mAh cm^{-2}) are significant, which may limit the composite electrode's practical use as a combined counter/reference electrode. Illustrating the impact of microstructure further, self-symmetric cells of cast alloys containing 50% by volume InLi within an indium metal matrix (Figure S14) were assembled and tested. Even at a low current density of 0.3 mA cm^{-2}, the extracted capacity was very small as only the lithium in the surface islands of InLi is accessible (Figure S14).[15] This highlights the impact of the electrode microstructure on performance in solid-state electrodes.

Cycling of indium−lithium electrodes. Based on the unidirectional chronopotentiometry data, a high current density and near-limit capacity of 3 mA cm^{-2} and a capacity of 3 mAh cm^{-2} were selected to investigate cycle stability. These challenging conditions were selected to allow the identification and mechanistic understanding of electrode performance degradation during cycling. Figure 4 shows cycling data for a self-symmetric two-electrode cell assembled with 70 mg of InLi intermetallic and indium foil on each side, cycled at a temperature of 303 K and a stack pressure of 5 MPa. Before cycling, the cell was rested for 24 h, with EIS taken every 2 h showing excellent stability in both potential and impedance (Figure S16). The cell was at OCV for 1 h after each charge and each discharge step including a 20 min EIS measurement. The working electrode is discharged (Li stripped) first. Figure 4A shows that 60 cycles are achieved before a voltage limit of 2.5 V is reached on the discharge cycle. Up to 50 cycles, the overpotentials are low even with such a high current density. Overall, the cycling data show a progressive worsening of performance instead of a sudden failure.

Figure 4B,C shows EIS data collected following each discharge and charge cycle, respectively. In line with the cycling potential data, there is a progressive increase in impedance after each discharge cycle. With the high-frequency tail excluded from the fit, the simple equivalent circuit model, inset in Figure 4D, fit the data well; this approximation simplifies the analysis compared to using a TLM for each of the two electrodes. The electrode resistance term in all 119 impedance curves is plotted in Figure 4D. The electrode resistance (R_{el}) grows progressively over successive cycles. The bulk resistance is approximately constant (Figure S17), which suggests that interfacial contact is maintained over successive cycles and is not the main mechanism of performance degradation.

The mean electrode resistance value was constant during the OCV, with a mean value of 2.31 Ω cm^2 (Figure S16). This reflects the pristine state of the InLi layers and therefore near-perfect ionic conductivity. The electrode resistance after each charge and discharge, divided by this value, is plotted in Figure 4E. The value decreases near-linearly with cycle number, indicating a progressive change in the electrode microstructure on successive cycles. Despite the composition of the electrodes after each cycle being identical, the microstructural distribution of the indium within the electrode progressively evolves such that ionic transport is impeded. After the final cycle, where a threshold potential of 2.5 V is reached, this ratio is below 10%.

Electrodes operating in the InLi|In two-phase region are effective counter/reference electrodes. The potential profile at very high currents on both charge and discharge is effectively flat. The electrodes should play a helpful role in accelerating research into electrode materials for solid-state batteries. The diffusion kinetics in the InLi intermetallics are incredibly fast, whereas the diffusion kinetics in the In metal phase are very slow. Lithium transport within the electrode is therefore dependent on the microstructure, which evolves as a result of lithiation/delithiation. The microstructural evolution, and therefore accessible capacity, depends on the current density due to the fundamental balance between transport and phase transformation kinetics. The addition of solid electrolyte particles into the electrode allows for a greater volume of indium metal to nucleate and grow within the fast diffusing InLi while maintaining a continuous ion conducting network, enabling greater extracted capacities than those achieved for a pure InLi layer. An optimal composition can be selected to balance the capacity, cycle stability, and flatness of the potential profile during discharge.

The coupled problem of indium precipitation and transport within the electrode seems ideal for a phase field model to describe. This could guide further improvement of this electrode and guide the understanding of two-phase solid-state anodes in general. Future work on this system could involve tracking the evolving microstructure using X-ray tomography operando at a range of discharge/charge rates.

Our work shows that InLi electrodes cycle stably, despite the use of porous cold-pressed electrolytes. Given the fundamental resistance of InLi|In electrodes to lithium plating, it would be misleading to use them in solid electrolyte development studies to demonstrate cycling stability. The role of a dense solid electrolyte is to control the morphology of deposited lithium metal and prevent dendrite-driven shorting. Going forward, these works should continue to use lithium metal and aim to achieve good rate capability by optimizing the electrolyte manufacturing method. Until this is widely achieved, using InLi|In as a counter/reference electrode can accelerate the development of solid-state cathodes and lithium-free anodes.

Considering alloys more broadly, intermetallics are an interesting and understudied materials class for lithium batteries; with unique mechanical, chemical, and transport properties. Their successful implementation as part of solid-state battery anodes requires understanding the effect of an evolving microstructure on the electrochemical performance. There are analogous lithium-rich intermetallics with very high diffusivity, which have an equilibrium two-phase region with lithium metal. Fast discharge performance superior to that of lithium metal may be achieved if electrodes can be made by incorporating these materials.

■ ASSOCIATED CONTENT

Supporting Information

The Supporting Information is available free of charge at https://pubs.acs.org/doi/10.1021/acsenergylett.3c02274.

Experimental methods. Figure S1 Ball-milled InLi powder. Figure S2 PFG-NMR data. Figure S3 CSM indentation data. Figure S4 Cube corner indentation with description. Figure S5 Open-circuit potential of InLi|In vs Li^+/Li. Figure S6 XRD of partially lithiated

https://doi.org/10.1021/acsenergylett.3c02274
ACS Energy Lett. 2024, 9, 578−585

indium foil. Figure S7 In foil first cycle potentiometry. Figures S8−S10 Reaction between Li and In foils to form electrodes. Figure S11 Potentiometry with varied areal loading of InLi powder. Figure S12 Potentiometry of CT cell. Table S1 Transmission-line model calculated values. Figure S13 InLilSSE composite electrochemical performance with description. Figures S14−S15 Cast two-phase alloy microstructure and performance with description. Figure S16 Impedance spectroscopy at OCV of two-layer electrode with description. Figure S17 Bulk resistance with cycle number (PDF)

AUTHOR INFORMATION

Corresponding Author

Mauro Pasta − *Department of Materials, University of Oxford, Oxford OX1 3PH, United Kingdom; The Faraday Institution, Didcot OX11 0RA, United Kingdom;* orcid.org/0000-0002-2613-4555; Email: mauro.pasta@materials.ox.ac.uk

Authors

Jack Aspinall − *Department of Materials, University of Oxford, Oxford OX1 3PH, United Kingdom; The Faraday Institution, Didcot OX11 0RA, United Kingdom*

Yvonne Chart − *Department of Materials, University of Oxford, Oxford OX1 3PH, United Kingdom; The Faraday Institution, Didcot OX11 0RA, United Kingdom*

Hua Guo − *Department of Materials, University of Oxford, Oxford OX1 3PH, United Kingdom; The Faraday Institution, Didcot OX11 0RA, United Kingdom*

Pranay Shrestha − *Department of Materials, University of Oxford, Oxford OX1 3PH, United Kingdom; The Faraday Institution, Didcot OX11 0RA, United Kingdom*

Matthew Burton − *Department of Materials, University of Oxford, Oxford OX1 3PH, United Kingdom; The Faraday Institution, Didcot OX11 0RA, United Kingdom;* orcid.org/0000-0002-0376-6322

Complete contact information is available at: https://pubs.acs.org/10.1021/acsenergylett.3c02274

Author Contributions

Jack Aspinall: Conceptualization, Methodology, Investigation, Writing - Original Draft, Reviewing and Editing. Yvonne Chart: Investigation. Hua Guo: Investigation. Pranay Shrestha: Investigation. Matthew Burton: Investigation. Mauro Pasta: Conceptualization, Methodology, Writing - Reviewing and Editing, Supervision, Project administration, Funding acquisition.

Notes

The authors declare no competing financial interest.

ACKNOWLEDGMENTS

This work was supported by the Faraday Institution [grant numbers FIRG056, FIRG058]. Equipment including the PI 88 nanoindenter and electron microscope was funded by the Henry Royce Institute (through UK Engineering and Physical Science Research Council grant EP/R010145/1). The X-ray microscope, software, and workstation used for the tomography and digital volume correlation analysis were supported by EPSRC Grant EP/M02833X/1"University of Oxford: experimental equipment upgrade".

REFERENCES

(1) Janek, J.; Zeier, W. G. A solid future for battery development. *Nature Energy* **2016**, *1*, 16141.

(2) Pasta, M.; et al. 2020 roadmap on solid-state batteries. *JPhys. Energy* **2020**, *2*, No. 032008.

(3) Cheng, E. J.; Sharafi, A.; Sakamoto, J. Intergranular Li metal propaga- tion through polycrystalline Li6.25Al0.25La3Zr2O12 ceramic electrolyte. *Electrochim. Acta* **2017**, *223*, 85−91.

(4) Ning, Z.; et al. Visualizing plating-induced cracking in lithium-anode solid- electrolyte cells. *Nat. Mater.* **2021**, *20*, 1121−1129.

(5) Kasemchainan, J.; et al. Critical stripping current leads to dendrite forma- tion on plating in lithium anode solid electrolyte cells. *Nat. Mater.* **2019**, *18*, 1105−1111.

(6) Kim, S.; Chart, Y. A.; Narayanan, S.; Pasta, M. Thin Solid Electrolyte Separators for Solid-State Lithium-Sulfur Batteries. *Nano Lett.* **2022**, *22*, 10176−10183.

(7) Aspinall, J.; Armstrong, D. E.; Pasta, M. EBSD coupled indentation: Nanoscale mechanics of lithium metal. *Materials Today Energy* **2022**, *30*, 101183.

(8) Kim, J.-S.; et al. Surface engineering of inorganic solid-state electrolytes via interlayers strategy for developing long-cycling quasi-all-solid-state lithium batteries. *Nat. Commun.* **2023**, *14*, 782.

(9) Hao, H.; et al. Tuned Reactivity at the Lithium Metal−Argyrodite Solid State Electrolyte Interphase. *Adv. Energy Mater.* **2023**, *13*, 2301338.

(10) Janek, J.; Zeier, W. G. Challenges in speeding up solid-state battery development. *Nature Energy* **2023**, *8*, 230−240.

(11) Ren, Y.; et al. Oxide-Based Solid-State Batteries: A Perspective on Com- posite Cathode Architecture. *Adv. Energy Mater.* **2023**, *13*, 2201939.

(12) Krauskopf, T.; Hartmann, H.; Zeier, W. G.; Janek, J. Toward a Funda- mental Understanding of the Lithium Metal Anode in Solid-State Batteries- An Electrochemo-Mechanical Study on the Garnet-Type Solid Electrolyte Li 6.25 Al 0.25 La 3 Zr 2 O 12. *ACS Appl. Mater. Interfaces* **2019**, *11*, 14463−14477.

(13) Ning, Z.; et al. Dendrite initiation and propagation in lithium metal solid- state batteries. *Nature* **2023**, *618*, 287−293.

(14) Santhosha, A. L.; Medenbach, L.; Buchheim, J. R.; Adelhelm, P. The Indium−Lithium Electrode in Solid-State Lithium-Ion Batteries: Phase Formation, Redox Potentials, and Interface Stability. *Batteries and Su- percaps* **2019**, *2*, 524−529.

(15) Jing, W.; et al. Li-Indium alloy anode for high-performance Li-metal bat- teries. *J. Alloys Compd.* **2022**, *924*, 166517.

(16) Luo, S.; et al. Growth of lithium-indium dendrites in all-solid-state lithium- based batteries with sulfide electrolytes. *Nat. Commun.* **2021**, *12*, 6968.

(17) Mallakpour, F.; Kasraie, M.; Herbert, E. G.; Phani, P. S.; Hackney, S. A. Length-scale-dependent stress relief mechanisms in indium at high homologous temperatures. *J. Mater. Res.* **2021**, *36*, 2444−2455.

(18) Lucas, B. N.; Oliver, W. C. Indentation power-law creep of high-purity indium. *Metallurgical and Materials Transactions A* **1999**, *30*, 601−610.

(19) Aspinall, J. et al. Lithium magnesium alloys: a framework for investigating lithium alloy anodes for solid state batteries. *Research Square*, 2023, Version 1.

(20) Tarczon, J. C.; Halperin, W. P.; Chen, S. C.; Brittain, J. O. Vacancy- antistructure defect interaction diffusion in β-LiAl and β-LiIn. *Mater. Sci. Eng. A* **1988**, *101*, 99−108.

(21) Qu, J.; Xiao, J.; Wang, T.; Legut, D.; Zhang, Q. High Rate Transfer Mechanism of Lithium Ions in Lithium-Tin and Lithium-Indium Alloys for Lithium Batteries. *J. Phys. Chem. C* **2020**, *124*, 24644−24652.

(22) Oliver, W.; Pharr, G. An improved technique for determining hardness and elastic modulus using load and displacement sensing indentation ex- periments. *J. Mater. Res.* **1992**, *7*, 1564−1583.

(23) Gibson, J. S. K.-L.; et al. Finding and Characterising Active Slip Systems: A Short Review and Tutorial with Automation Tools. *Materials* **2021**, *14*, 407.

(24) Lewis, J. A.; Cavallaro, K. A.; Liu, Y.; McDowell, M. T. The promise of alloy anodes for solid-state batteries. *Joule* **2022**, *6*, 1418−1430.
(25) Riegger, L. M.; et al. Evolution of the Interphase between Argyrodite- Based Solid Electrolytes and the Lithium Metal Anode—The Kinetics of Solid Electrolyte Interphase Growth. *Chem. Mater.* **2023**, *35*, 5091−5099.
(26) Siroma, Z.; et al. Mathematical solutions of comprehensive variations of a transmission-line model of the theoretical impedance of porous electrodes. *Electrochim. Acta* **2015**, *160*, 313−322.
(27) Braun, P.; Uhlmann, C.; Weiss, M.; Weber, A.; Ivers-Tiffée, E. Assess- ment of all-solid-state lithium-ion batteries. *J. Power Sources* **2018**, *393*, 119−127.
(28) Hertle, J.; et al. Miniaturization of Reference Electrodes for Solid-State Lithium-Ion Batteries. *J. Electrochem. Soc.* **2023**, *170*, No. 040519.
(29) Capone, I.; et al. A red phosphorus-graphite composite as anode material for potassium-ion batteries. *Materials Today Energy* **2021**, *21*, 100840.
(30) Lee, Y.-g.; et al. High-energy long-cycling all-solid-state lithium metal bat- teries enabled by silver−carbon composite anodes. *Nature Energy* **2020**, *5*, 299−308.
(31) Froboese, L.; Sichel, J. F. v. d.; Loellhoeffel, T.; Helmers, L.; Kwade, A. Effect of Microstructure on the Ionic Conductivity of an All Solid-State Battery Electrode. *J. Electrochem. Soc.* **2019**, *166*, A318−A328.

https://doi.org/10.1021/acsenergylett.3c02274
ACS Energy Lett. 2024, 9, 578−585